

# Synergistic Engineering of Defects and Architecture in Binary Metal Chalcogenide toward Fast and Reliable Lithium–Sulfur Batteries

Dan Luo, Gaoran Li, Ya-Ping Deng, Zhen Zhang, Jingde Li, Ruilin Liang, Matthew Li, Yi Jiang, Weiwei Zhang, Yangshuai Liu, Wen Lei, Aiping Yu, and Zhongwei Chen\*

Lithium–sulfur (Li–S) batteries have great promise to support the next-generation energy storage if their sluggish redox kinetics and polysulfide shuttling can be addressed. The rational design of sulfur electrodes plays key roles in tackling these problems and achieving high-efficiency sulfur electrochemistry. Herein, a synergetic defect and architecture engineering strategy to design highly disordered spinel Ni–Co oxide double-shelled microspheres (NCO-HS), which consist of defective spinel  $\text{NiCo}_2\text{O}_{4-x}$  ( $x = 0.9$  if all nickel is  $\text{Ni}^{2+}$  and cobalt is  $\text{Co}^{2.13+}$ ), as the multifunctional sulfur host material is reported. The in situ constructed cation and anion defects endow the NCO-HS with significantly enhanced electronic conductivity and superior polysulfide adsorbability. Meanwhile, the delicate nanoconstruction offers abundant active interfaces and reduced ion diffusion pathways for efficient Li–S chemistry. Attributed to these synergistic features, the sulfur composite electrode achieves excellent rate performance up to 5 C, remarkable cycling stability over 800 cycles and good areal capacity of  $6.3 \text{ mAh cm}^{-2}$  under high sulfur loading. This proposed strategy based on synergy engineering could also inform material engineering in related energy storage and conversion fields.

## 1. Introduction

Advanced energy storage technologies with high energy/power density and low cost have been attracting extensive research attentions to meet the ever-increasing energy demand.<sup>[1]</sup> Lithium–sulfur (Li–S) batteries are regarded as one of the most promising candidates for next-generation energy storage benefiting from the natural abundance, environmental benignity, and high specific capacity of sulfur.<sup>[2]</sup> While the significant advantages are convincing, the wide-scale commercialization of Li–S batteries is so far limited because of some intractable technical challenges, which involve the ionically and electrically insulating nature of sulfur, the dissolution and shuttling behaviors of the intermediate lithium polysulfides (LPS), and the large volume expansion during cycling.<sup>[3]</sup>

Under these circumstances, polar materials such as transitional metal chalcogenides (TMCs) have been developed as promising sulfur immobilizer for improved sulfur electrochemistry. The favorable interactions between TMCs and LPS strengthen the sulfur confinement within the cathode, while the nanostructure construction can further promote the reaction kinetics by offering decent ionic/electronic conductivity. Among TMCs,  $\text{Co}_3\text{O}_4$  has drawn particular research interests due to its high electrochemical stability and strong LPS adsorbability.<sup>[4]</sup> However, the relatively poor electron and ion conduction properties and low catalytic activity of  $\text{Co}_3\text{O}_4$  are greatly impeding its widespread implementation.<sup>[5]</sup> In this regard, defect engineering and morphology design have been regarded as promising strategies to efficiently accelerate Li–S chemistry. Cation and anion defects in TMCs have been reported capable of manipulating the electronic structure toward favorable physical and electrochemical properties, so affecting the energetics for electron and ion transport as well as adsorbability.<sup>[6]</sup> However, despite its successful applications in other chemistries, defect engineering has been rarely investigated for improving the kinetics and sulfur hosting capability of sulfur chemistry. A comprehensive understanding of defects in adsorption and electrocatalysis will shed light on the advanced sulfur host design in Li–S battery. Beyond that,

D. Luo, Dr. G. Li, Y.-P. Deng, Z. Zhang, R. Liang, M. Li, Dr. Y. Jiang, Dr. Y. Liu, Prof. A. Yu, Prof. Z. Chen  
Department of Chemical Engineering  
Waterloo Institute of Nanotechnology  
University of Waterloo  
200 University Ave West, Waterloo, Ontario N2L 3G1, Canada  
E-mail: zhwenchen@uwaterloo.ca

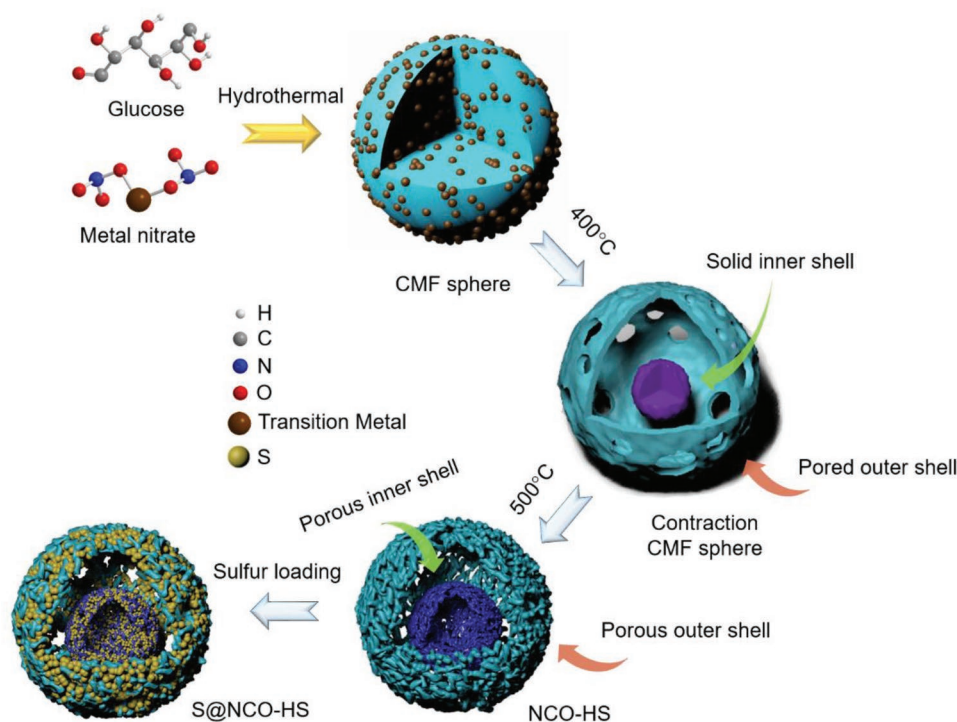
Prof. J. Li  
School of Chemical Engineering and Technology  
Hebei University of Technology  
Tianjin 300130, China

W. Zhang  
Department of Material Science Engineering  
McMaster University  
1280 Main Street West, Hamilton, Ontario L8S 4L8, Canada

Prof. W. Lei  
The State Key Laboratory of Refractories and Metallurgy  
Wuhan University of Science and Technology  
947 Heping Avenue, Wuhan 430081, China

 The ORCID identification number(s) for the author(s) of this article can be found under <https://doi.org/10.1002/aenm.201900228>.

DOI: 10.1002/aenm.201900228



**Scheme 1.** Illustration of the morphological evolution during the synthetic process of NCO-HS.

morphological tuning on TMCs also delivers critical impacts on the sulfur redox reaction by reducing LPS diffusion pathway and enhancing sulfur confinement.<sup>[7]</sup>

Herein, we present a synergistic strategy to optimize the structural and adsorptive properties of TMCs toward the specific demands of Li–S systems. This facile strategy involves the one-pot synthesis and the subsequent thermal treatment to yield highly defective TMCs hollow microspheres (TMCs-HS). As a demonstration, disordered spinel nickel cobalt oxide (Ni–Co oxide) double-shelled microspheres (NCO-HS), which consists highly defective spinel  $\text{NiCo}_2\text{O}_{4-x}$  ( $x = 0.9$  if all nickel is  $\text{Ni}^{2+}$  and cobalt is  $\text{Co}^{2.13+}$ ), was developed with abundant oxygen vacancies on octahedral sites. The defect engineering endows the NCO-HS with significantly enhanced electronic conductivity and alters the chemical interactions with LPS toward excellent sulfur immobilization. Moreover, the highly porous and double-shelled architecture shortens the ion transfer distance, homogenizes the sulfur distribution, offers abundant active interfaces, and buffers the volume variation. When employed it as sulfur host, these advantageous features enable high sulfur utilization, fast reaction kinetics, and strong sulfur confinement, leading to outstanding battery cyclability with an ultralow capacity fading rate of 0.045% per cycle over 800 cycles at 0.2 C (1 C = 1675 mA g<sup>-1</sup>) and remarkable rate capability up to 5 C, as well as a high areal capacity of 6.3 mAh cm<sup>-2</sup> under raised sulfur loading. This strategy offers a synergy of defects engineering and structural design that renders fast and durable sulfur electrochemistry as well as significantly improved battery performance, holding a great promise in promoting the practical application of Li–S batteries.

## 2. Result and Discussion

**Scheme 1** illustrates the synthetic process of NCO-HS and the according morphological evolution. NCO-HS with uniform size and morphology was synthesized through a one-step hydrothermal method followed by annealing treatment under air atmosphere. In this method, glucose and metal nitrates are mixed together for hydrothermal reactions, in which the metal ions ( $\text{Ni}^{2+}$  and  $\text{Co}^{2+}$ ) are adsorbed via an in situ coordinating process during the preliminary carbonization of glucose to form carbonaceous microspherical frameworks (CMFs).<sup>[8]</sup> **Figure 1A** shows the morphology of CMF with spherical shape and smooth surface. Subsequently, in the calcination process in air, the CMF microspheres began to shrink near 300 °C induced by the temperature gradient,<sup>[9]</sup> which is confirmed by scanning electron microscopy (SEM), transmission electron microscopy (TEM), and X-ray diffraction (XRD) (Figure S1A–C, Supporting Information). When the temperature continues increasing to 400 °C, the layer separation occurs inside the solid CMF sphere to form a double-shelled structure, which is attributed to the combined actions of contraction force and adhesion force in opposite directions on the shell.<sup>[10]</sup> (Figure S1D,E, Supporting Information) Meanwhile, the XRD pattern reveals the formation of crystalline Ni–Co oxide during this annealing stage (Figure S1F, Supporting Information), while the drastic weakening of the carbon peak indicates the decomposition of the carbonaceous components. At a higher temperature of 500 °C, the highly porous and hollow structured NCO-HS was collected through prolonged annealing as shown in Figure 1B,C.<sup>[11]</sup>

The obtained microspheres exhibit good size uniformity and plentiful mesopores on the shell surface, which is confirmed by

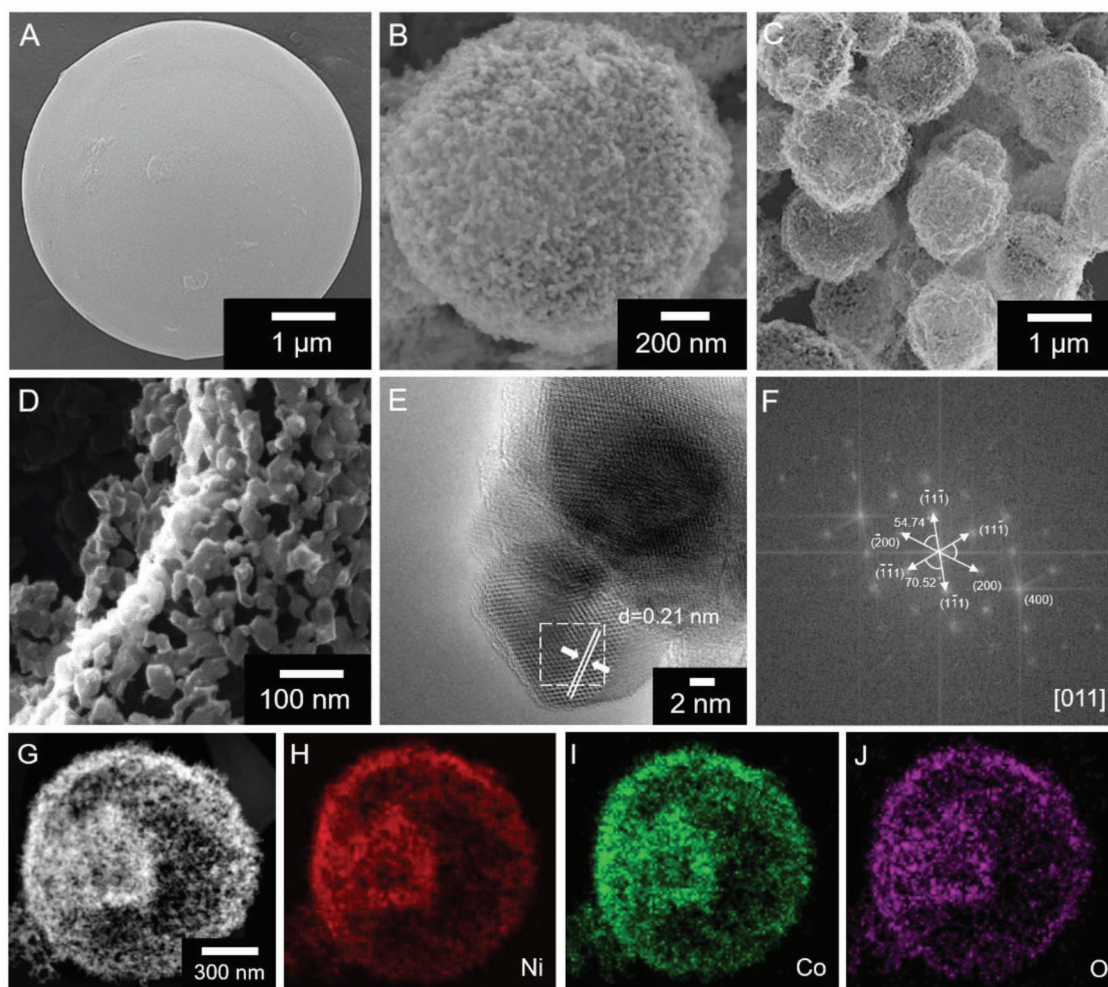


**Figure 1.** SEM images of A) single CMF, B) single particle of NCO-HS, and C) multiple particles of NCO-HS. D) SHIM image, E) HRTEM image, and F) FFT images of NCO-HS. G) STEM image and H–J) element distribution mapping of Ni, Co, and O for NCO-HS.

scanning helium ion microscopy (SHIM), indicating its good electron and ion transportation.<sup>[12]</sup> Clearly, the highly porous NCO-HS acquires good structure integrity without any damage or malposition when bombarded by He ions (Figure 1D). The highly porous shells in NCO-HS provide vast active sites for sulfur reaction as well as abundant channels for ion transfer, while the large inner voids in the hollow structure could facilitate sufficient sulfur loading. The STEM images of NCO-HS and energy dispersive X-ray (EDX) element distribution clearly reveal its interior structure and uniform element distribution (Figure 1H–J). The element distribution of carbon and thermogravimetric analysis (TGA) in Figure S2 of the Supporting Information revealed the formation of TMCs without excessive carbon remaining.<sup>[13]</sup> It should be noted that this synthetic method delivers good universality and can be extended to various hollow structured TMCs. As for demonstration, other TMCs such as  $\text{Co}_3\text{O}_4$  and NiO double-shelled hollow microspheres ( $\text{Co}_3\text{O}_4$ -HS and NiO-HS) were successfully synthesized by simply tuning the composition of the carbonaceous precursor (Figure S3, Supporting Information). Such a facile and universal synthetic strategy is promising for the structural designs of TMCs to meet specific demands in a wide range of potential application fields.

The in-depth crystalline feature of the obtained NCO-HS was further characterized by HRTEM, which exhibits an interplanar spacing of 0.21 nm corresponding to the (400) crystallographic plane (Figure 1E). Meanwhile, the fast Fourier transform (FFT) image with periodic arrangement of the lattice fringe selected area (Figure 1F) reveals a cubic structure with a crystal axis of [011]. Figure 2A shows the XRD result of NCO-HS, confirming its cubic spinel phase with the  $Fd\bar{3}m$  space group.<sup>[14]</sup> For comparison, the  $\text{Co}_3\text{O}_4$ -HS was also prepared *via* the same method but without defects. The XRD pattern and FFT image implies its similar crystal structures with NCO-HS (Figure 2A; Figure S4, Supporting Information). However, the significantly broadened and negatively shifted XRD peaks as well as reduced lattice fringe from FFT can be observed for NCO-HS, suggesting an disordered lattice volume resulted from defect engineering.<sup>[15]</sup> The NCO-HS exhibits a high Brunauer–Emmett–Teller surface area of  $102.2 \text{ m}^2 \text{ g}^{-1}$  and hierarchical pore size distribution (Figure S5, Supporting Information). The high porosity and large surface area built into the microstructure are beneficial for uniform distribution of sulfur, efficient confinement of LPS, and fast ion/electron transfer during the charge–discharge process.

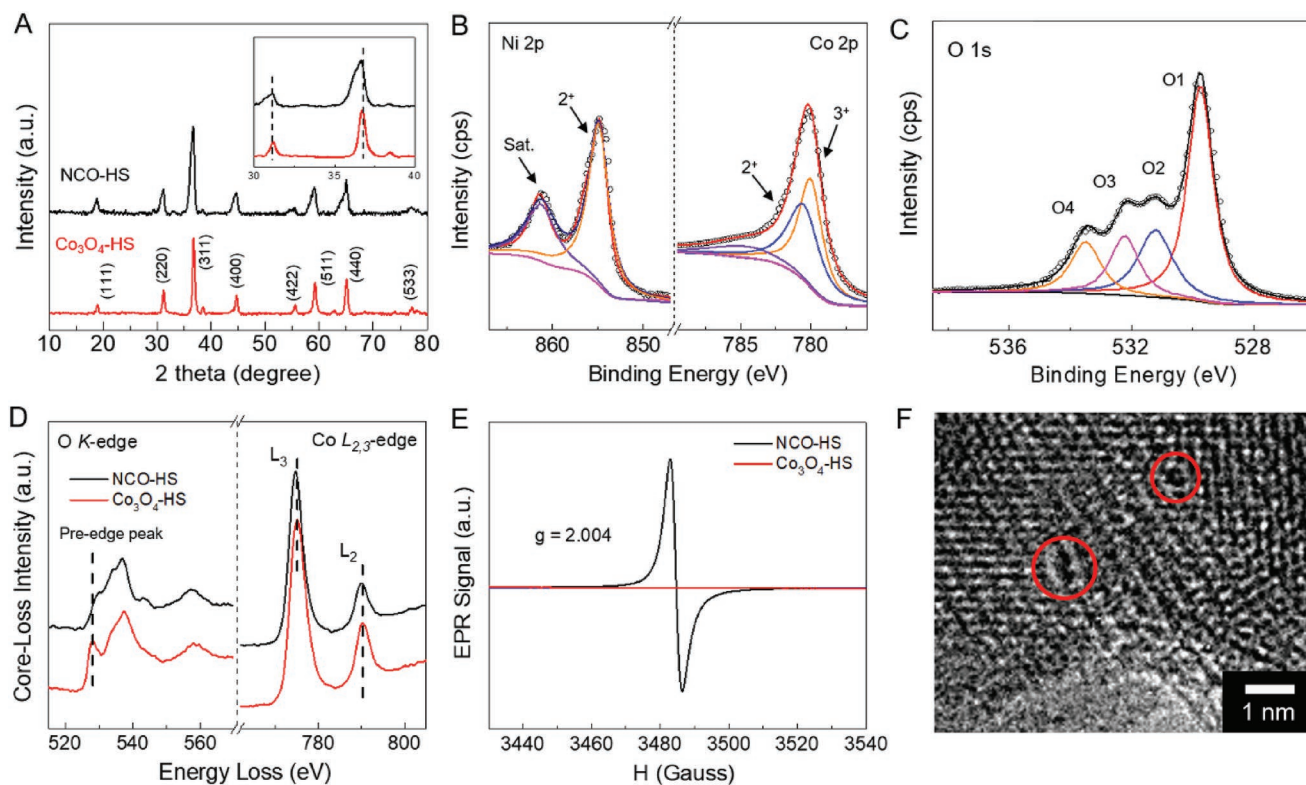


**Figure 2.** A) XRD patterns of NCO-HS and  $\text{Co}_3\text{O}_4$ -HS (inset: local magnification of the (220) and (311) peaks); the high resolution B) Ni 2p and Co 2p and C) O 1s XPS spectra of NCO-HS. D) ELNES spectra of the O K-edge and Co  $L_{2,3}$ -edges and E) EPR pattern of NCO-HS and  $\text{Co}_3\text{O}_4$ -HS. F) TEM image of defective sites on NCO-HS.

Beyond that, the defect engineering strategy by substituting Ni into the spinel  $\text{Co}_3\text{O}_4$  lattice is expected to increase the electrical conductivity and intensify the interactions between TMCs and sulfur species.<sup>[16]</sup> In order to investigate the defective structure in NCO-HS, the chemical composition of the product was confirmed by inductively coupled plasma optical emission spectrometry (ICP-OES), which indicates a Ni/Co ratio of 0.5 (Table S1, Supporting Information). The surface chemistry of NCO-HS was investigated by X-ray photoelectron spectroscopy (XPS) analysis. The peaks located at 854.7 eV in Ni  $2p_{3/2}$  spectrum (Figure 2B) confirms the existence of  $\text{Ni}^{2+}$  species in NCO-HS.<sup>[17]</sup> The two sub peaks in Co  $2p_{3/2}$  spectrum located at 780 and 780.7 eV can be assigned to  $\text{Co}^{3+}$  and  $\text{Co}^{2+}$ , which implies the nonintegral valence of cobalt in NCO-HS.<sup>[18]</sup> Figure 2C displays the O 1s spectrum of NCO-HS, which can be fitted into four sub peaks (O1, O2, O3, and O4). The strongest O1 peak is located at 529.8 eV, corresponding to metal–oxygen bonds.<sup>[19]</sup> A shoulder O2 peak can be observed at 531.2 eV, indicating the hydroxylated surface of NCO-HS, which is favorable to attracting LPS.<sup>[20]</sup> The O3 peak at 532.2 eV can be considered to be defects with a low oxygen coordination.<sup>[21]</sup> The O4 peak located at 533.5 eV is contributed by adsorbed moisture on the surface of NCO-HS.<sup>[22]</sup> The defective structure of NCO-HS was further probed by electron energy loss near-edge structure spectroscopy (ELNES), electron paramagnetic response spectroscopy (EPR) and HRTEM. Figure 2D shows the core-loss O K-edge and Co  $L_{2,3}$ -edges near-edge spectra. The pre-edge peak located at 528 eV in O K-edge spectra is attributed

to the hybridization of the unoccupied O 2p orbital with Co 3d orbitals.<sup>[23]</sup> The less prominent pre-edge peak of NCO-HS confirming the existence of oxygen vacancies.<sup>[24]</sup> In Co  $L_{2,3}$ -edges spectra, the intense  $L_3$  edge can be assigned to Co  $2p_{3/2}$  and the  $L_2$  edge is attributed to Co  $2p_{1/2}$  orbital. A 0.5 eV shift is observed from the Co  $L_3$  peak of NCO-HS while the Co  $L_2$  peak remains unchanged, indicating the valence state reduction of octahedral  $\text{Co}^{3+}$  species.<sup>[25]</sup> This shift is in good agreement with the trend observed from Co  $2p_{3/2}$  XPS spectra (Figure S6A,B, Supporting Information), which exhibits a positive shift of 0.4 eV binding energy (BE) of  $\text{Co}^{3+}$  peak in NCO-HS compared with  $\text{Co}_3\text{O}_4$ -HS. The processed ELNES spectrum reveals an  $L_3/L_2$  intensity ratio of 4.21, implying the valence state around  $\text{Co}^{2.2+}$  (Figure S7A, Supporting Information).<sup>[26]</sup> Moreover, the normalized Co  $L_{2,3}$  ELNES spectrum regression fitting in Figure S7B of the Supporting Information suggest a composition of 20.5% of  $\text{Co}_3\text{O}_4$  (with  $\text{Co}^{2.67+}$ ) and 79.5% of CoO (with  $\text{Co}^{2+}$ ), indicating the cobalt valence state in NCO is  $\text{Co}^{2.13+}$ . This ELNES fitting result also indicates the formation of disordered octahedral coordination around Co sites in NCO-HS. As a result, the ELNES, XRD, XPS, and ICP analyses cooperatively indicate the formation of highly disordered spinel NCO-HS in formula of  $\text{NiCo}_2\text{O}_{4-x}$  ( $x = 0.9$  if all nickel is  $\text{Ni}^{2+}$ , oxygen is  $\text{O}^{2-}$ , and cobalt is  $\text{Co}^{2.13+}$ ).<sup>[27]</sup> The EPR pattern present a distinctive EPR signal with a g value of 2.004, suggesting a higher concentration of oxygen vacancies in NCO-HS in drastic contrast to  $\text{Co}_3\text{O}_4$ -HS (Figure 2E).<sup>[28]</sup> Besides, defective sites in NCO-HS can be clearly observed from lattice fringes in HRTEM images,

as shown in Figure 2F. All these results consistently verify the highly defective nature of the as-developed NCO-HS.

The defect engineering is expected to create new defect states such as dangling bonds and oxygen vacancies located in the band gap of  $\text{Co}_3\text{O}_4$  so as to lower the formation energy of electron holes in  $\text{Co}_3\text{O}_4$  and give rise to a substantially enhanced electrical conductivity.<sup>[29]</sup> To examine the boosted electrical conductivity through defect-engineering in the proposed strategy, the conductivity of the prepared NCO-HS,  $\text{Co}_3\text{O}_4$ -HS, and  $\text{Co}_3\text{O}_4$ -NPs were measured. The as-developed NCO-HS exhibits a significantly higher conductivity of  $0.52 \text{ S cm}^{-1}$  and such electrical conductivity enhancement of NCO-HS is expected to offer an improved electron transfer for fast sulfur electrochemistry. Overall, the above evidences reveal that cation and anion defects have been successfully constructed in NCO-HS, which favors the electron conduction for facilitated sulfur redox reactions.

In view of its highly defective and polar nature, NCO-HS could also facilitate the adsorption of LPS for improved sulfur confinement in Li-S batteries.<sup>[30]</sup> To testify the LPS adsorption abilities, NCO-HS,  $\text{Co}_3\text{O}_4$ -HS, and  $\text{Co}_3\text{O}_4$ -NPs were immersed into  $4 \times 10^{-3} \text{ M}$   $\text{Li}_2\text{S}_6$  solution for comparison (Figure 3A). After adsorption, the  $\text{Li}_2\text{S}_6$  solution adsorbed by NCO-HS exhibits more transparent color than the others, which intuitively illustrates its strongest adsorption to LPS. UV-vis measurements were performed to further investigate the  $\text{Li}_2\text{S}_6$  adsorption capabilities. The UV-vis spectrum of the pristine  $\text{Li}_2\text{S}_6$  shows peaks at 265 and 415 nm, which is corresponded to  $\text{S}_6^{2-}$  and  $\text{S}_4^{2-}$ .<sup>[31]</sup> The intensities of these peaks are in positive correlation with the LPS concentration in solutions.<sup>[32]</sup> The peaks for

NCO-HS specimen experience the largest decrease in intensity, indicating its strongest adsorption to polysulfides. The as-developed NCO-HS delivers the highest polysulfide adsorption capability of 1.763 mg  $\text{Li}_2\text{S}_6$  per 5 mg material, as shown in Figure 3B and Figure S8. XPS analysis was performed to verify these chemical interactions. It can be clearly observed that both the Co  $2p_{1/2}$  and Co  $2p_{3/2}$  peaks of NCO-HS/LPS shift significantly to lower BE ranges (Figure S6A, Supporting Information). Especially, the octahedral coordinated Co peak undergoes a much large shift than that for  $\text{Co}_3\text{O}_4$ -HS/LPS (Figure S6B, Supporting Information). These results strongly support that the introduction of defect engineering in NCO-HS improves the chemical interaction between Co and LPS.<sup>[33]</sup> Besides, the major peak of the M-O bond in NCO-HS/LPS shifts to a higher BE range, corresponding to a reduction of electron cloud density in O, suggesting the formation of “lithium bond”-like interactions (Figure S6C, Supporting Information).<sup>[34]</sup> The other peaks in the NCO-HS/LPS O1s spectra shift toward lower BE, which implies the coordination between the defective oxygen and the sulfur in LPS, corresponding to the adsorption of polysulfides on oxygen vacancies.<sup>[35]</sup> Further verification on the chemical interactions can be gained through the S 2p XPS spectra (Figure 3C). The large shift of  $\text{S}_T^{-1}$  and  $\text{S}_B^0$  peaks in the NCO-HS/LPS spectra can be observed after adsorbed  $\text{Li}_2\text{S}_6$ , indicating the reduction of electron cloud density in sulfur atoms and further confirming the strong chemical interactions between NCO-HS and LPS.<sup>[36]</sup> This is attributed to the stronger binding ability and the increased adsorption sites induced by the massive oxygen vacancies in NCO-HS.<sup>[37]</sup>

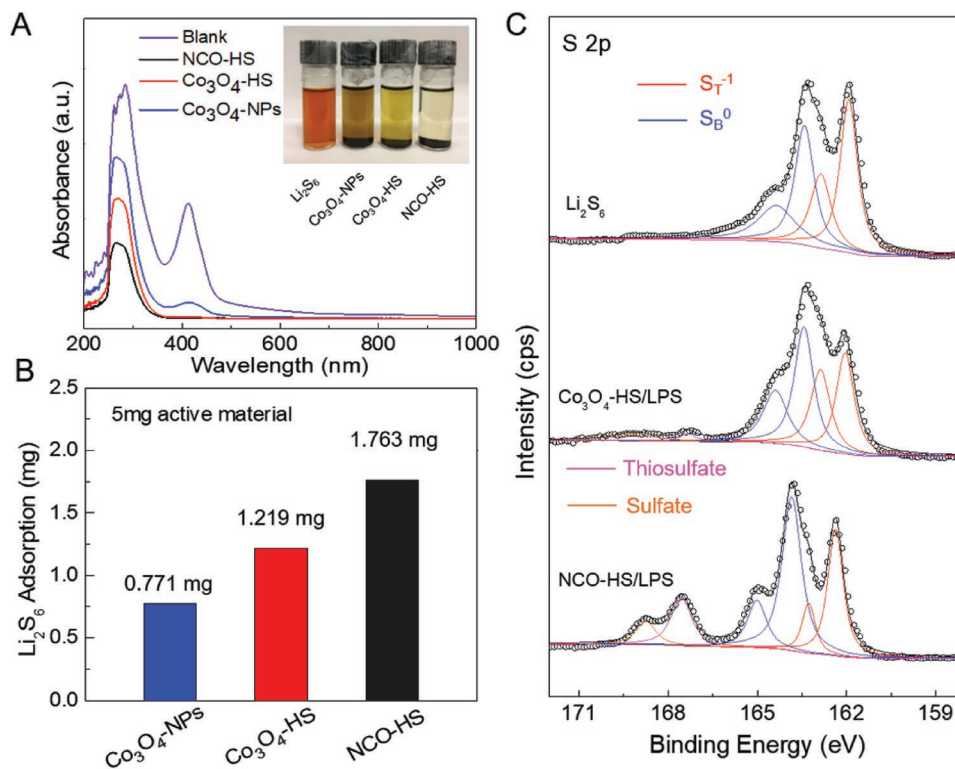


**Figure 3.** A) UV-vis spectra and optical images of LPS solutions adsorbed by  $\text{Co}_3\text{O}_4$ -NPs,  $\text{Co}_3\text{O}_4$ -HS, and NCO-HS. B) The polysulfide adsorption capacities of different adsorbers. C) XPS spectra of S 2p for pristine  $\text{Li}_2\text{S}_6$ ,  $\text{Co}_3\text{O}_4$ -HS/LPS, and NCO-HS/LPS.

A pair of new peaks emerges at the higher BE in NCO-HS/LPS spectra, which refers to the formation of polythionate complex and further manifests the chemical bondage between defective sites of NCO-HS and LPS.<sup>[38]</sup> All these variations in XPS spectra evidentially support the strong chemical interactions between NCO-HS and sulfur species.

The interactions between LPS and metal oxide surfaces were calculated by density functional theory (DFT+U) calculations based on the Vienna ab initio simulation package.<sup>[39]</sup> The results show that LPS@NCO exhibits a higher BE, indicating a stronger interaction between NCO and LPS, which is presented in Figure S9 of the Supporting Information. Moreover, a significantly reduced Li–O (1.86 Å) and Co–S (2.20 Å) bond distances can be obtained in LPS@NCO (Figure S9F, Supporting Information), which is consistent with the XPS results and suggest the much-strengthened Li–O and metal–sulfur binding of NCO.

Symmetrical cells were further employed to investigate the interfacial interaction of polysulfide.<sup>[40]</sup> The cyclic voltammetry (CV) data and EIS results of different symmetrical cells are shown in Figure S10 of the Supporting Information. It can be clearly observed that the NCO-HS sample exhibits the highest redox current density and smallest electrochemical resistance among the different electrodes. These results further confirm the significantly improved kinetics of polysulfides redox reactions on NCO-HS matrix, which is attributed to its superior conductivity and stronger LPS adsorption.<sup>[41]</sup>

Electrochemical measurement were further performed to verify the Li–S battery performance. TMCs-sulfur composites were prepared with a sulfur content of 70 wt% in the composites,<sup>[42]</sup> which is confirmed by TGA analysis in Figure S11 of the Supporting Information. The peaks ascribed to elemental sulfur can be clearly observed in the XRD pattern (Figure S12, Supporting Information), indicating the successful impregnation of sulfur in NCO-HS, Co<sub>3</sub>O<sub>4</sub>-HS, and Co<sub>3</sub>O<sub>4</sub>-NPs. The SEM and TEM image in Figure S13 of the Supporting Information indicates a uniform distribution of sulfur. After sulfur loading, the NCO-HS sphere well maintains its structure without collapses. For comparison, the morphology of Co<sub>3</sub>O<sub>4</sub>-HS and Co<sub>3</sub>O<sub>4</sub>-NPs and their sulfur composites are also provided in Figure S14 of the Supporting Information, which exhibits more sulfur agglomeration than NCO-HS. Also, the strong sulfur peak in XRD pattern indicates the high crystallinity of sulfur, revealing the existence of bulk sulfur particle. The severe sulfur agglomeration significantly impedes charge and mass transfer and enable the composite electrode with poor Li–S electrochemical performance. Besides, the N<sub>2</sub> adsorption–desorption isotherms of NCO-HS undergoes a drastic decrease after sulfur loading (Figure S15, Supporting Information), confirming the occupation of sulfur in the pores. These results demonstrate the successful sulfur loading and the uniform sulfur distribution.

Electrochemical evaluations were conducted to verify the advantageous effects of NCO-HS serving as sulfur immobilizer for Li–S batteries. Figure 4A shows the typical galvanostatic charge–discharge profiles with two distinguished plateaus curves for all the S@NCO-HS, S@Co<sub>3</sub>O<sub>4</sub>-HS, and S@Co<sub>3</sub>O<sub>4</sub>-NPs electrodes (corresponding to sulfur composite electrodes based on NCO-HS, Co<sub>3</sub>O<sub>4</sub>-HS and Co<sub>3</sub>O<sub>4</sub>-NPs, respectively). The discharge plateau at around 2.3 V (vs Li<sup>+</sup>/Li) is related

to the electroreduction of sulfur into long-chain LPS (Li<sub>2</sub>S<sub>8</sub> and Li<sub>2</sub>S<sub>6</sub>), while the other discharge plateau at around 2.1 V corresponds to the further reduction of the LPS to Li<sub>2</sub>S<sub>2</sub> and Li<sub>2</sub>S. The CV results in Figure 4B are in good agreement with the charge–discharge profiles by showing two major reduction peaks at 2.3 and 2.05 V, and two major oxidation peaks at 2.35 and 2.4 V. Notably, the S@NCO-HS electrode displays the smallest potential hysteresis in both charge–discharge profiles and CV curve compared to the other electrodes, indicating its smaller electrochemical polarization and improved reaction kinetics. The rate performances in Figure 4C and Figure S16 (Supporting Information) show that the S@NCO-HS electrode exhibits the best rate capability with a high discharge capacity of 855 mAh g<sup>−1</sup> at 5 C as well as a highly reversible capacity of 1103.5 mAh g<sup>−1</sup> when the current is returned to 0.2 C. Even under raised current density, the charge–discharge curves of S@NCO-HS still displays two distinguished plateaus curves without severe potential hysteresis and delivers the highest discharge capacity among those composites. These results manifest that the defect engineering on NCO-HS can provide favorable conduction properties for the sulfur electrode to achieve fast reaction kinetics.

Figure 4D shows the cycling performances of different electrodes at 0.2 C. The S@NCO-HS electrode exhibits the best cycling performance with a high capacity retention of 1143.8 mAh g<sup>−1</sup> after 100 cycles. Benefited from the structural superiorities of NCO-HS, which combining strong physical and chemical adsorptions of LPS, a superior cyclability of S@NCO-HS electrode can be achieved. The highly reversible capacity and stable coulombic efficiency can be obtained from cycling performance in Figure S17 of the Supporting Information, indicating the strong confinement of LPS and the expedite sulfur electroreactions in S@NCO-HS. The sulfur confinement in S@NCO-HS was further revealed by SEM observation (Figure S18, Supporting Information). The uniform coating of sulfur species on the NCO-HS surface after 100 cycles indicates the strong sulfur immobilization and inhibited polysulfide shuttling for S@NCO-HS electrode. By contrast, the platelet-like crystalline Li<sub>2</sub>S can be clearly observed on Co<sub>3</sub>O<sub>4</sub>-HS after cycling, signifying a relatively severe dissolution and shuttling behaviors of LPS. After cycling, the NCO-HS well maintains its unique morphology without structural damage or cracks (Figure S19, Supporting Information). The EDX elemental mapping also reveals a uniform element distribution of Ni, Co, O, and S in the electrode (Figure S20, Supporting Information). The highly porosity on the shell provide enough space to store sulfur and buffer the volume change during charge–discharge process. These results reveal the strong structural integrity of NCO-HS to tolerate the volume expansion during lithiation/delithiation. Considering its high porosity, large inner voids, and great structural stability, electrochemical performance of sulfur electrodes based on S@NCO-HS composites with different sulfur contents were also investigated. Benefited from the structural superiorities, sulfur was uniformly distributed on the subunits of NCO-HS even at a high sulfur content up to 80 wt% (Figure S21, Supporting Information). The cyclic performances of S@NCO-HS electrodes with different sulfur content (Figure S22, Supporting Information) indicates that the composite with 70 wt% sulfur exhibits the highest discharge capacity and cyclability, which can be employed for further

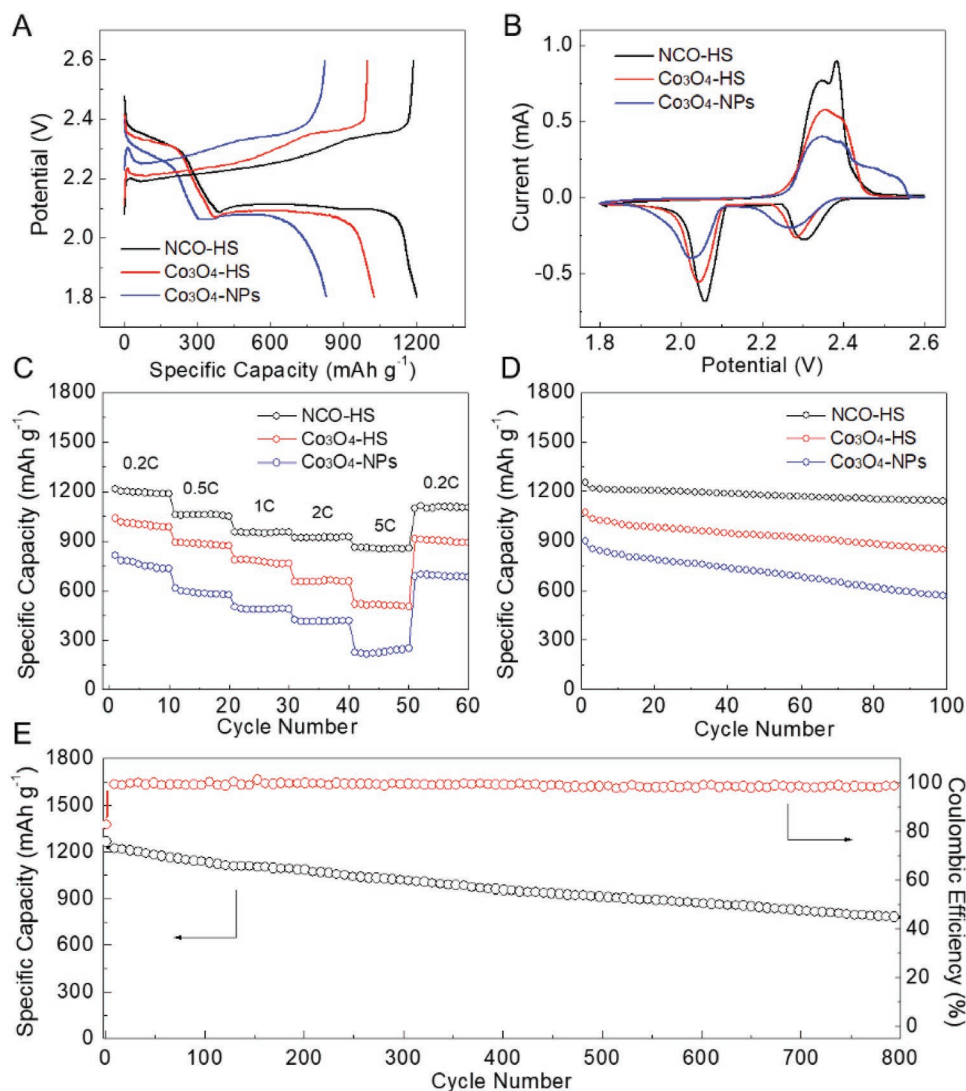


**Figure 4.** A) Galvanostatic discharge–charge profiles at 0.2 C, B) CV curves at scan rate of  $0.1 \text{ mV s}^{-1}$ , C) rate performances, and D) cycling performances at 0.2 C of S@NCO-HS, S@Co<sub>3</sub>O<sub>4</sub>-HS, and S@Co<sub>3</sub>O<sub>4</sub>-NPs electrodes. E) Specific capacity and coulombic efficiency of S@NCO-HS electrode over the long-term cycling at 0.2 C.

long-term cycling measurements. Attributed to the uniform sulfur distribution, favored reaction kinetics, and enhanced sulfur immobilization, the S@NCO-HS electrode achieves an outstanding cyclability with a low capacity fading rate of 0.045% per cycle and a highly reversible capacity of  $781.8 \text{ mAh g}^{-1}$  after 800 cycles at 0.2 C (Figure 4E). A high rate cycling test of the S@NCO-HS composite electrode was also performed at 1.0 C for 300 cycles, as shown in Figure S23 of the Supporting Information. The S@NCO-HS electrode retains a highly reversible capacity of  $790.3 \text{ mAh g}^{-1}$  after 300 cycles as well as a high coulombic efficiency over the cycling. These results are highly competitive among sulfur electrodes based on metal oxides host in Table S2 of the Supporting Information, strongly supporting the intriguing structural superiorities of NCO-HS as an advanced sulfur host for Li–S batteries.

To further understand the underlying mechanism of the performance enhancement of the S@NCO-HS electrode, a series of electrochemical analyses was performed to verify the benefits

of NCO-HS in terms of ion and electron transportation. The defective NCO nanosized subunits establish a 3D conductive architecture while the porous hollow structure offers enlarged electrode/electrolyte interfaces and multi-dimensional channels for ion diffusion (Figure 5A). Therefore, S@NCO-HS composites guarantee sufficient ion supply and fast sulfur electrochemical redox. The above argument receives strong support from the potentiostatic intermittent titration (PITT), which shows that the S@NCO-HS electrode delivers the highest  $\text{Li}^+$  diffusion coefficient ( $D_{\text{Li}^+}$ ) (Figure 5B). The  $D_{\text{Li}^+}$  in discharge and charge processes are in good correspondence, revealing the good reversibility of these composite electrodes. The high  $D_{\text{Li}^+}$  of S@NCO-HS is benefited from the high porosity and large inner voids in the architecture, which offer abundant  $\text{Li}^+$  pathways for  $\text{Li}^+$  diffusion. Conductivity measurements and EIS tests were also performed to verify the improved sulfur electroredox for S@NCO-HS. Notably, S@NCO-HS still possess the highest conductivity of  $0.29 \text{ S cm}^{-1}$  after loading 70 wt% sulfur,

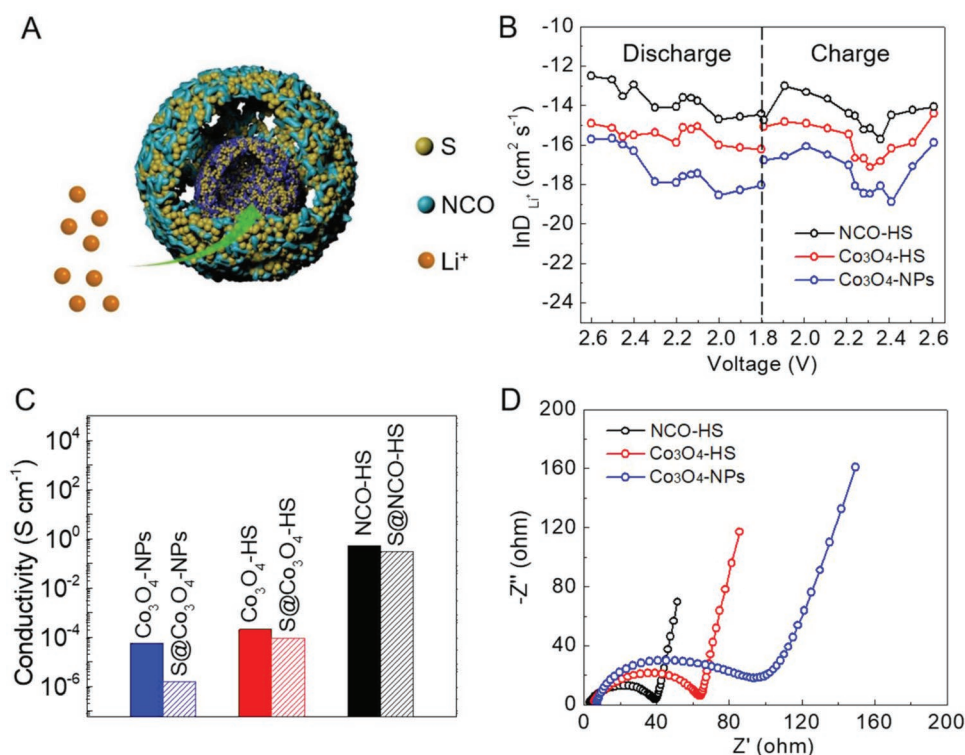


**Figure 5.** A) Schematic illustration of kinetic features of S@NCO-HS. B) PITT profiles reveal the Li<sup>+</sup> diffusion coefficients of S@NCO-HS, S@Co<sub>3</sub>O<sub>4</sub>-HS, and S@Co<sub>3</sub>O<sub>4</sub>-NPs upon the discharge–charge process. C) The electrical conductivities of NCO-HS, Co<sub>3</sub>O<sub>4</sub>-HS, and Co<sub>3</sub>O<sub>4</sub>-NPs, and their sulfur composites. D) EIS spectra of S@NCO-HS, S@Co<sub>3</sub>O<sub>4</sub>-HS, and S@Co<sub>3</sub>O<sub>4</sub>-NPs electrodes.

indicating the best electron transfer within the bulk composite (Figure 5C). Moreover, Figure 5D shows the Nyquist plots of different sulfur electrodes at the fully charged state. Clearly, S@NCO-HS holds the smallest interfacial charge-transfer resistance and Warburg resistance, which further illustrates its best charge and mass transfer properties among these three composites. These results are in good agreement with the PITT profiles and rate performances, evidencing the great promotion of conduction properties and the sulfur electrochemical reaction kinetics contributed by the unique structural features of NCO-HS.

To examine the structure differentiation affected by Ni content, NCO-HS with different Ni/Co ratio was synthesized and characterized by XRD in Figure S24 of the Supporting Information. With the increase of Ni content, the XRD peak of NCO-HS shifts more toward lower angle, indicating severe structure change and result in higher content of oxygen vacancies. Especially, the major XRD peak of NiCo<sub>2</sub>O<sub>4-x</sub> undergoes the largest shift from 36.83° to 36.66°, indicating the highly disordered spinel structure that NiCo<sub>2</sub>O<sub>4-x</sub> possessed among those materials, leading to the formation of abundant oxygen vacancies in octahedral sites. The S@NCO-HS composites with different nickel substitution were prepared and their electrochemical performance is shown in Figure S25 of the Supporting Information, the first discharge–charge cycle of those samples was measured at a current density of 0.2 C with different Ni content. The discharge–charge profiles exhibit a higher discharge plateau, lower potential hysteresis, and higher discharge capacity with the nickel content increasing. Moreover, the conductivity of NCO-HS significantly improves with Ni content increasing.<sup>[43]</sup>

Benefitting from those advantages, the S@NiCo<sub>2</sub>O<sub>4-x</sub> cathode exhibits the highest initial discharge capacity. However, with the Ni/Co ratio further increasing, NiO phase will formed in NCO-HS during CMF calcination. The NiO dissolution caused severe structure deformation, oxygen vacancies compensation, and conductivity loss of NCO-HS.<sup>[44]</sup> As a result, the S@Ni<sub>1.5</sub>Co<sub>1.5</sub>O<sub>4-x</sub> cathode exhibits poor conductivity, low PS adsorbability and finally demonstrates a relatively low discharge capacity.

Self-discharge behavior is a significant indicator of LPS shuttling effect. The self-discharge evaluation was performed by resting the composite electrodes at 2.2 V in their second discharge for 24 h (Figure S26, Supporting Information). The results show that the S@NCO-HS electrode exhibits the lowest voltage decay during battery rest and demonstrates the best capacity retention of 94.4% after rest, which strongly confirms its superior LPS shuttling inhibition.

The practical application of Li–S batteries requires a raised sulfur loading of sulfur electrode for higher energy density. Figure 6A shows the galvanostatic charge–discharge curves of S@NCO-HS electrode at different current densities. Clearly, the distinguished two-plateau charge–discharge curves can still be obtained at a relatively high rate of 2 C, indicating its low polarization and good reaction kinetics even under high sulfur loading. Nevertheless, Figure 6B manifests the good rate capability of the high-loading S@NCO-HS electrode by showing a highly reversible areal capacity of 3.8 mAh cm<sup>-2</sup> at 2 C and a decent capacity of 5.4 mAh cm<sup>-2</sup> after switching the current back to 0.2 C. Furthermore, the stable long-term operation also indicates the good cyclability of the S@NCO-HS electrode

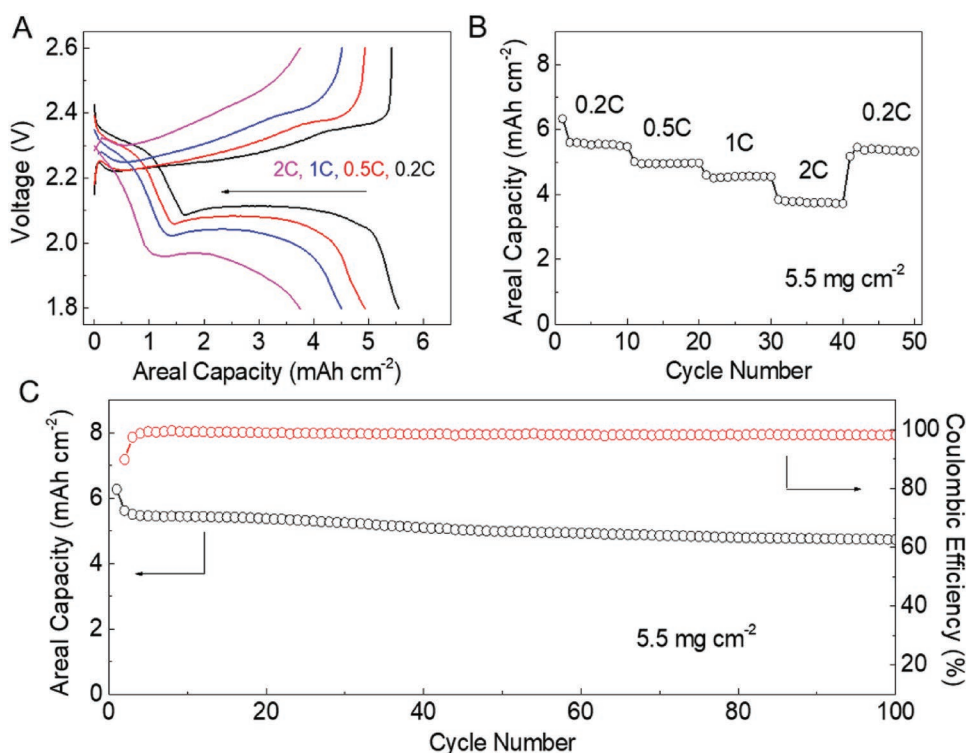


**Figure 6.** A) Charge–discharge profiles at different current densities and B) rate performance of S@NCO-HS electrode with a sulfur loading of 5.5 mg cm<sup>-2</sup>. C) The areal capacities and coulombic efficiency of S@NCO-HS electrode at over 100 cycles 0.2 C.

under high sulfur loading (Figure 6C) with a constantly high areal capacity over 5 mAh cm<sup>-2</sup>, which is competitive with commercial Li-ion batteries.<sup>[45]</sup> The good electrochemical performance under raised sulfur loading is attributed to the synergistically combined morphological and structural superiorities of NCO-HS. The uniform sulfur distribution and the excellent conduction properties in the highly porous and defective NCO-HS ensures high sulfur utilization and fast reaction kinetics, while the strong physical and chemical sulfur immobilizations further suppress the dissolution and shuttling behaviors of polysulfide, leading to significantly prolonged cycling lifespan.

### 3. Conclusion

In summary, we have developed a facile synergistic strategy to synthesize TMC-HS employed with abundant cation and anion defects. The obtained NCO-HS displays a unique double-shelled hollow structure and hierarchical porosity, which favors uniform sulfur distribution, fast ion transfer, and good physical sulfur confinement. Meanwhile, the defective spinel NCO-HS consisting abundant Ni<sup>2+</sup> substitution within Co<sub>3</sub>O<sub>4</sub>-HS matrix and oxygen vacancies on octahedral sites, was endowed with significantly enhanced ionic/electronic conductivity and strong chemical interactions with sulfur species, contributing to fast sulfur electroredox and excellent sulfur immobilization. Benefited from these advantages, S@NCO-HS achieves fast and durable sulfur electrochemistry with a minimal capacity fading rate of 0.045% per cycle over 800 cycles, superior rate capability up to 5 C, and high areal capacity of 6.3 mAh cm<sup>-2</sup> under raised sulfur loading.

This implementation of synergistic engineering to design highly conductive and adsorptive multifunctional sulfur host offers an instructive attempt for material engineering toward superior Li–S performance, which also paves way for other energy storage applications such as electrocatalysis and supercapacitors.

### Supporting Information

Supporting Information is available from the Wiley Online Library or from the author.

### Acknowledgements

D.L. and G.L. contributed equally to this work. This research work was supported by the Natural Science and Engineering Research Council of Canada (NSERC) and the University of Waterloo. The authors would also like to thank Dr. Carmen Andei from Canadian Centre for Electron Microscopy at McMaster University for TEM characterizations.

### Conflict of Interest

The authors declare no conflict of interest.

### Keywords

defects, facile synthesis, lithium–sulfur batteries, metal chalcogenide

Received: January 20, 2019

Revised: February 28, 2019

Published online:

- [1] a) J. Xie, H. J. Peng, J. Q. Huang, W. T. Xu, X. Chen, Q. Zhang, *Angew. Chem., Int. Ed.* **2017**, *56*, 16223; b) G. Li, D. Luo, X. Wang, M. H. Seo, S. Hemmati, A. Yu, Z. Chen, *Adv. Funct. Mater.* **2017**, *27*, 1702562; c) D. Luo, C. J. Wallar, K. Y. Shi, I. Zhitomirsky, *Colloids Surf., A* **2016**, *509*, 504.
- [2] a) W. Zhou, C. Wang, Q. Zhang, H. D. Abruña, Y. He, J. Wang, S. X. Mao, X. Xiao, *Adv. Energy Mater.* **2015**, *5*, 1401752; b) Z. Li, Q. He, X. Xu, Y. Zhao, X. Liu, C. Zhou, D. Ai, L. Xia, L. Mai, *Adv. Mater.* **2018**, *30*, 1804089.
- [3] a) B. Y. Guan, A. Kushima, L. Yu, S. Li, J. Li, X. W. D. Lou, *Adv. Mater.* **2017**, *29*, 1605902; b) G. Li, S. Wang, Y. Zhang, M. Li, Z. Chen, J. Lu, *Adv. Mater.* **2018**, *30*, 1705590.
- [4] a) J. Wang, N. Yang, H. Tang, Z. Dong, Q. Jin, M. Yang, D. Kisailus, H. Zhao, Z. Tang, D. Wang, *Angew. Chem., Int. Ed.* **2013**, *52*, 6417; b) L. Hu, Q. Peng, A. Y. Li, *J. Am. Chem. Soc.* **2008**, *130*, 16136.
- [5] a) D. R. Deng, F. Xue, Y. J. Jia, J. C. Ye, C. D. Bai, M. S. Zheng, Q. F. Dong, *ACS Nano* **2017**, *11*, 6031; b) H. Cheng, S. Wang, D. Tao, M. Wang, *Funct. Mater. Lett.* **2014**, *07*, 1450020.
- [6] a) D. Chen, M. Qiao, Y. R. Lu, L. Hao, D. Liu, C. L. Dong, Y. Li, S. Wang, *Angew. Chem., Int. Ed.* **2018**, *57*, 8691; b) M. Zhao, H. J. Peng, Z. W. Zhang, B. Q. Li, X. Chen, J. Xie, X. Chen, J. Y. Wei, Q. Zhang, J. Q. Huang, *Angew. Chem., Int. Ed.* **2019**, *131*, 1.
- [7] W. Zhou, Y. Yu, H. Chen, F. J. DiSalvo, H. D. Abruña, *J. Am. Chem. Soc.* **2013**, *135*, 16736.
- [8] M. M. Titirici, M. Antonietti, A. Thomas, *Chem. Mater.* **2006**, *18*, 3808.
- [9] Z. Ma, X. Yuan, L. Li, Z.-F. Ma, L. Zhang, L. Mai, J. Zhang, *J. Power Sources* **2015**, *291*, 156.
- [10] L. Shen, L. Yu, X. Y. Yu, X. Zhang, X. W. Lou, *Angew. Chem., Int. Ed.* **2015**, *54*, 1868.
- [11] D. Luo, Y. P. Deng, X. Wang, G. Li, J. Wu, J. Fu, W. Lei, R. Liang, Y. Liu, Y. Ding, A. Yu, Z. Chen, *ACS Nano* **2017**, *11*, 11521.
- [12] a) V. Iberi, I. Vlasiouk, X. G. Zhang, B. Matola, A. Linn, D. C. Joy, A. J. Rondinone, *Sci. Rep.* **2015**, *5*, 11952; b) D. Emmrich, A. Beyer, A. Nadzeyka, S. Bauerdick, J. C. Meyer, J. Kotakoski, A. Götzhäuser, *Appl. Phys. Lett.* **2016**, *108*, 163103.
- [13] B. Li, X. Ge, F. W. Goh, T. S. Hor, D. Geng, G. Du, Z. Liu, J. Zhang, X. Liu, Y. Zong, *Nanoscale* **2015**, *7*, 1830.
- [14] Y. Ren, Z. Ma, P. G. Bruce, *Chem. Soc. Rev.* **2012**, *41*, 4909.
- [15] X. Yao, Y. Ke, W. Ren, X. Wang, F. Xiong, W. Yang, M. Qin, Q. Li, L. Mai, *Adv. Energy Mater.* **2019**, *9*, 1803260.
- [16] a) C. Wei, Z. Feng, G. G. Scherer, J. Barber, Y. Shao-Horn, Z. J. Xu, *Adv. Mater.* **2017**, *29*, 1606800; b) X. Tong, X. Xia, C. Guo, Y. Zhang, J. Tu, H. J. Fan, X.-Y. Guo, *J. Mater. Chem. A* **2015**, *3*, 18372.
- [17] D. McNulty, H. Geaney, C. O'Dwyer, *Sci. Rep.* **2017**, *7*, 42263.
- [18] a) G. Li, W. Lei, D. Luo, Y. Deng, Z. Deng, D. Wang, A. Yu, Z. Chen, *Energy Environ. Sci.* **2018**, *11*, 2372; b) J. Zhou, N. Lin, W. Cai, C. Guo, K. Zhang, J. Zhou, Y. Zhu, Y. Qian, *Electrochim. Acta* **2016**, *218*, 243; c) R. Tang, C. Jiang, W. Qian, J. Jian, X. Zhang, H. Wang, H. Yang, *Sci. Rep.* **2015**, *5*, 13645.
- [19] L. Xu, Q. Jiang, Z. Xiao, X. Li, J. Huo, S. Wang, L. Dai, *Angew. Chem., Int. Ed.* **2016**, *55*, 5277.
- [20] C. Yuan, J. Li, L. Hou, X. Zhang, L. Shen, X. W. D. Lou, *Adv. Funct. Mater.* **2012**, *22*, 4592.
- [21] a) R. Gao, Z. Li, X. Zhang, J. Zhang, Z. Hu, X. Liu, *ACS Catal.* **2016**, *6*, 400; b) T. Choudhury, S. O. Saied, J. L. Sullivan, A. M. Abbot, *J. Phys. D: Appl. Phys.* **1989**, *22*, 1185.
- [22] Z. Ju, G. Ma, Y. Zhao, Z. Xing, Y. Qiang, Y. Qian, *Part. Part. Syst. Charact.* **2015**, *32*, 1012.
- [23] K. Luo, M. R. Roberts, N. Guerrini, N. Tapia-Ruiz, R. Hao, F. Massel, D. M. Pickup, S. Ramos, Y. S. Liu, J. Guo, A. V. Chadwick, L. C. Duda, P. G. Bruce, *J. Am. Chem. Soc.* **2016**, *138*, 11211.
- [24] J. Suntiovich, W. T. Hong, Y.-L. Lee, J. M. Rondinelli, W. Yang, J. B. Goodenough, B. Dabrowski, J. W. Freeland, Y. Shao-Horn, *J. Phys. Chem. C* **2014**, *118*, 1856.
- [25] J. Fu, F. M. Hassan, C. Zhong, J. Lu, H. Liu, A. Yu, Z. Chen, *Adv. Mater.* **2017**, *29*, 1702526.
- [26] Z. L. Wang, J. S. Yin, Y. D. Jiang, *Micron* **2000**, *31*, 571.
- [27] G. L. Xu, Y. F. Xu, J. C. Fang, F. Fu, H. Sun, L. Huang, S. Yang, S. G. Sun, *ACS Appl. Mater. Interfaces* **2013**, *5*, 6316.
- [28] Y. Zhang, Z. Mu, C. Yang, Z. Xu, S. Zhang, X. Zhang, Y. Li, J. Lai, Z. Sun, Y. Yang, Y. Chao, C. Li, X. Ge, W. Yang, S. Guo, *Adv. Funct. Mater.* **2018**, *28*, 1707578.
- [29] a) Y. Wang, T. Zhou, K. Jiang, P. Da, Z. Peng, J. Tang, B. Kong, W.-B. Cai, Z. Yang, G. Zheng, *Adv. Energy Mater.* **2014**, *4*, 1400696; b) T. Zhou, Y. Zheng, H. Gao, S. Min, S. Li, H. K. Liu, Z. Guo, *Adv. Sci.* **2015**, *2*, 1500027.
- [30] Y. Zhong, K. R. Yang, W. Liu, P. He, V. Batista, H. Wang, *J. Phys. Chem. C* **2017**, *121*, 14222.
- [31] a) C. Barchasz, F. Molton, C. Duboc, J. C. Lepretre, S. Patoux, F. Alloin, *Anal. Chem.* **2012**, *84*, 3973; b) J. Tan, D. Liu, X. Xu, L. Mai, *Nanoscale* **2017**, *9*, 19001.
- [32] W. Cai, G. Li, K. Zhang, G. Xiao, C. Wang, K. Ye, Z. Chen, Y. Zhu, Y. Qian, *Adv. Funct. Mater.* **2018**, *28*, 1704865.
- [33] Q. Pang, D. Kundu, L. F. Nazar, *Mater. Horiz.* **2016**, *3*, 130.
- [34] a) L. Kong, X. Chen, B. Q. Li, H. J. Peng, J. Q. Huang, J. Xie, Q. Zhang, *Adv. Mater.* **2018**, *30*, 1705219; b) T. Z. Hou, W. T. Xu, X. Chen, H. J. Peng, J. Q. Huang, Q. Zhang, *Angew. Chem., Int. Ed.* **2017**, *56*, 8178.
- [35] a) Y. Liu, G. Li, Z. Chen, X. Peng, *J. Mater. Chem. A* **2017**, *5*, 9775; b) J. Hwang, R. R. Rao, L. Giordano, Y. Katayama, Y. Yu, Y. Shao-Horn, *Science* **2017**, *358*, 751.
- [36] G. Li, W. Lei, D. Luo, Y.-P. Deng, D. Wang, Z. Chen, *Adv. Energy Mater.* **2018**, *8*, 1702381.
- [37] a) X. Liu, J. Q. Huang, Q. Zhang, L. Mai, *Adv. Mater.* **2017**, *29*, 1601759; b) Z. Liang, G. Y. Zheng, W. Y. Li, Z. W. Seh, H. B. Yao, K. Yan, D. S. Kong, Y. Cui, *ACS Nano* **2014**, *8*, 5249.
- [38] Q. Pang, X. Liang, C. Y. Kwok, L. F. Nazar, *Nat. Energy* **2016**, *1*, 16132.
- [39] G. Kresse, J. Furthmüller, *Phys. Rev. B* **1996**, *54*, 11169.
- [40] Y. Y. Mi, W. Liu, X. L. Li, J. L. Zhuang, H. H. Zhou, H. L. Wang, *Nano Res.* **2017**, *10*, 3698.
- [41] Z. Yuan, H. J. Peng, T. Z. Hou, J. Q. Huang, C. M. Chen, D. W. Wang, X. B. Cheng, F. Wei, Q. Zhang, *Nano Lett.* **2016**, *16*, 519.
- [42] Z. Z. Yang, H. Y. Wang, L. Lu, C. Wang, X. B. Zhong, J. G. Wang, Q. C. Jiang, *Sci. Rep.* **2016**, *6*, 22990.
- [43] X. Shi, S. L. Bernasek, A. Selloni, *J. Phys. Chem. C* **2017**, *121*, 3929.
- [44] S. Kuboon, Y. H. Hu, *Ind. Eng. Chem. Res.* **2011**, *50*, 2015.
- [45] L. Miao, W. Wang, K. Yuan, Y. Yang, A. Wang, *Chem. Commun.* **2014**, *50*, 13231.